Check for updates

COMPUTATIONAL DESIGN OF ALLOYS FOR ENERGY TECHNOLOGIES

# Crack Formation in Chill Block Melt Spinning Solidification Process: A Comparative Analysis Using OpenFOAM®

M.R. PAGNOLA ●,[1,2,5] F. BARCELÓ,[3] and J. USECHE[4]

1.—Laboratorio de Sólidos Amorfos, Facultad de Ingeniería, Universidad de Buenos Aires, Av, Paseo Colon 850, C1063ACV Buenos Aires, Argentina. 2.—Instituto de Tecnologías y Ciencias de la Ingeniería "Hilario Fernández Long" (INTECIN), CONICET - Universidad de Buenos Aires, Buenos Aires, Argentina. 3.—Instituto de Tecnología (INTEC), Universidad Argentina de la Empresa (UADE), Lima 717, C1073AAO Ciudad Autónoma de Buenos Aires, Buenos Aires, Argentina. 4.—Facultad de Ingeniería, Universidad Tecnológica de Bolívar, Parque Industrial y Tecnológico Carlos Vélez Pombo, km 1 vía Turbaco, CP 130010 Cartagena, Colombia. 5.—e-mail: mpagnola@gmail.com

The application of FeSiB family magnetic materials in the electrical or electronic industry has significantly increased owing to the development of amorphous and nanocrystalline metallic glasses using melt spinning and chill block melt spinning technology, which involves a rotating metal wheel with a high rotation speed. With this technique, a thin ribbon is obtained owing to the jet of liquid metal expelled from a casting nozzle at high pressure and temperature over the outer surface of the wheel. The cooling rates that can be achieved lead to disorder in the crystalline lattice of the metal, which is dependent on the chemical composition. As soon as the material jet is expelled by the nozzle, turbulence can occur in the solidification puddles. This generates defects and cracks in the solidification profile. In this study, numerically simulated ad hoc events in OPENFOAM® are comparatively examined using a real process.

## INTRODUCTION

It is estimated that, worldwide, about 2% of the total electrical energy generated is lost in distribution transformers. There is potential to increase the energy efficiency of a transformer by reducing these losses through the deployment of new alloys with improved magnetic behavior.[1] In this sense, the development of amorphous and nanocrystalline alloys reduces the vacuum losses of these cores by up to 80%.[2,3] However, the stacking factor of these ribbons in the core is important as any defect, such as a crack or trapped air bubble, will reduce the efficiency.[4] Wang and Matthys[5] present the boundary layer theory to model the solidification process of the puddle in melt spinning. Steen and Karcher[6] present a broad discussion of flow stability, which influences the movement of the meniscus, final texture, and instability of the morphological type of

the solidification front, but this work presents a computational study that tries to show the origin of these defects to help reduce them and obtain more efficient amorphous cores. Commonly FeSiB alloys are used to obtain amorphous magnetic alloy ribbons via melt spinning. To obtain nanocrystalline structures, we can incorporate alloys such as Cu, Nb, and Ti[7,8] or perform thermally controlled treatments.[9] The present study is focused on the $Fe_{78}Si_9B_{13}$ alloy (at.%) ejected with a gap of 2 mm over a rotating copper wheel. This process is called chill block melt spinning (CBMS) and has been examined in previous studies.[10–12] This technique is used to produce small thickness metallic ribbons and can lead to a variety of technological applications. If the rotational speed in the copper wheel exceeds 30 m s$^{-1}$, vortices can be formed. These can form irregularities in the ribbon's profile due to gas trapping at the metal solidification interface.[13] The atmosphere surrounding the molten puddle can reach speeds in the range of 12–14 m s$^{-1}$, especially at the beginning of the process and before the ejection flow of the molten material stabilizes. These

values define the vorticity in the contact zone, thereby showing their effect on the coefficient of heat transfer via convection when $Bi_{S/l}$ (Biot number in the solid–liquid interface) $> 1$ and $Bi_A$ (Biot number in the solid–air interface) $> 7.2 \times 10^{-4}$.[14] During the cooling of the ribbon over the course of its phase change, these vorticities can lead to small rifts that propagate according to a mechanism. We describe this mechanism in the present study.

## EXPERIMENTAL

### Laboratory Test

The FeSiB ingot production process was conducted according to the procedure reported by Pagnola et al.[11] The process was set up for a gap of 2 mm with a wheel rotation speed ($V_x$) of approximately 40 m s$^{-1}$. Under similar conditions, the temperature profile was established in the ejection column of the molten material, and temperature changes were analyzed.[15] In the present study, a decrease in temperature was observed at a rate of approximately $-9.3 \times 10^6$ K s$^{-1}$ near the critical length (Lcr $\sim 6.8 \times 10^{-4}$ m) of the system.[16] This implies temperatures in the range of 300–400°C in the contact areas of the alloy with the wheel, which is in the proximity of the critical length (Lcr). The values in this range were obtained by Barone et al.[17] in similar process conditions. Under the conditions of flow instability described in "Introduction" section, irregularities appear on the ribbon's surface along with changes in width and thickness. These irregularities can be due to gas entrapment at the liquid–wheel interface, which locally results in less efficient cooling of the adjacent metal[13,18] and can generate rifts on the solidification surface. This defect is observed in Fig. 1 via optical microscopy of the obtained laboratory ribbon profile. For process values with R $>$ 210, the meniscus does not form, and other defects, such as the typical "balloon"-shaped particles, appear.[17,19]

Specifically,

$$R = \frac{Vx.\text{tc}}{Z - Lcr} \qquad (1)$$

where Vx = wheel speed [m s$^{-1}$], Tc = critical nucleation time [s], $Z$ = characteristic length of the ejection hole [m], Lcr = critical length [m].

For the value of Z/W[20] close to unity [corresponding to the ribbon width W (m)], we obtained a ribbon with dimensions specified in Fig. 1b, where the profile formation with irregular sections can be observed because it is close to the previously mentioned instability zone. Notwithstanding the irregularities, an average width (W) for this relationship of $0.717 \times 10^{-3}$ m can be determined with a thickness of 32 $\mu$m and roughness in the range of 0.85–2.75 $\mu$m. Similar values in this range have been observed by other authors.[13,16,21,22]



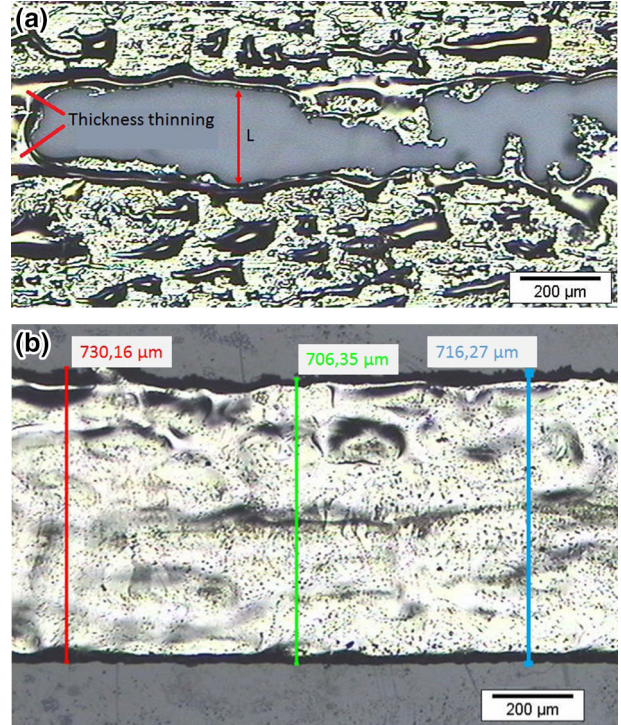Fig. 1. Optical microscopy of rifts on Fe$_{78}$Si$_9$B$_{13}$ ribbon (at.%) obtained in the melt spinning process: (a) width (L): $1.7 \times 10^{-4}$ m–$2.5 \times 10^{-4}$ m; (b) average width (W): $0.717 \times 10^{-3}$ m.

### Numerical Modeling

Numerical modeling was conducted with the setup parameters described in "Laboratory Test" section, which were assigned to a model previously implemented in OPENFOAM® for the liquid phase,[14] and it was later improved with the implementation of the volume of fluid (VOF) model for two non-isothermal, immiscible, and compressible fluids. The transportation equation that controls the movement of the free surface is given by:

$$\frac{\partial \Phi}{\partial t} + \nabla.(\Phi v) = \frac{d\Phi}{dt} + \Phi.(\nabla v) = 0 \qquad (2)$$

where $\Phi$ is the volume of fluid function (VOF), which is a discontinuous function that measures the amount of fluid present in a volume element taking values between 0 (if the volume of fluid does not contain molten material) and 1(when the volume contains entirety molten material), and v is the velocity field. The equation that governs the phenomenon of molten metal flow in the melt spinning process is given by the mass balance equation:

$$\nabla.v = 0 \qquad (3)$$

A compressible model is selected solely to use OpenFOAM's framework for thermal physical models. CompressibleInterFoam allows programming a viscous model to represent phase changes in the alloy and considers heat exchange between the alloy and surrounding air. Nevertheless, the density for

both fluids is considered constant. The boundary conditions in the process were treated in Refs. 14, 16, considering there is a non-slip and non-penetration flow condition in the solid surfaces of the injection and wheel nozzle. On the surface of the wheel, the fluid moves at the same speed as the wheel. CompressibleInterFoam solver was used to solve the mathematical model with an improved Vogel-Fulcher-Tammann (V-F-T)-type viscosity function (HTE model), which was previously designed and assigned to solve thermophysical models.[15,17] The obtained thicknesses of the solidified ribbon with the HTE model have a reasonable relative error value in the range of speeds of interest between 10 and 40 m s$^{-1}$, as is contrasted with experimental values reported in Fig. 2.

The post-processing of images was done with the ParaView® software, and the visualization of the simulation results with a gap of 2 mm and wheel rotation speed ($V_x$) of approximately 40 m s$^{-1}$ allows observation of the formation of the puddle and cracking defects described in "Introduction and Laboratory Test" section (see Fig. 3).

The obtained profile shows the temperature distribution of the mass of the molten metal that begins to solidify on the cooled wheel (lower plane in Fig. 3). We use the profile to examine the mechanism of crack formation on the cold surface and obtain cross sections (Si with $i = 0$–15) along the largest crack observed in the figure with an approximate length of 0.54 mm. We commence from the coldest section (downstream or right) of the profile. Each section is separated from the other section by 0.1 mm as measured along an axis centered on the median plane of the illustrated profile. In the results, only the main sections are shown and correspond to $S_4$, $S_5$, $S_8$, and $S_{11}$.

## Viscosity Treatment

The relationship between the viscosities of the metal as a function of the temperature (T) during the phase change is estimated based on a hyperbolic tangent equation (HTE) in the glass transition temperature ($T_{tg}$) environment, and it can be obtained via Eq. 4. The functions are executed in a Matlab/Octave routine reported by Barone et al.[17]

$$\mu(T) = \frac{1}{2}\mu_{\max}\{1 + \tanh[\alpha(T_{tg} + \delta - T)]\} \quad (4)$$

where $\mu_{\max} = 1.76 \times 10^{14}$ Pa s, $\alpha = 0.14104$, $\delta = 109.18$.

The solid-state region is defined as the portion of fluid with a viscosity $> 1 \times 10^{14}$ kg m$^{-1}$ s$^{-1}$ (see Fig. 4).[20,23]

## RESULTS AND DISCUSSION

### Results

The results are presented in the form of the main cross sections. Specifically, the thickness plane, temperature plane, and viscosity plane obtained in each region of analysis are shown in different figures. Hence, we commence the simulation by considering a section ahead of section $S_4$ prior to the formation of the crack in $S_4$ (see Figs. 2 and 3). Furthermore, section $S_{11}$ is considered the final section near the casting pool.

### General Discussion

Figure 5a shows the ribbon cross-sectional profile with a width of 0.71 mm and an average thickness of 28.3 $\mu$m. The thickness in the central part decreases to 27 $\mu$m.

In Fig. 5b, the temperature field is observed on the same cross section at 280°C in the contact area with the cold surface. The temperature increases at higher planes and corresponds to 1100°C in the upper part of the cross section. Furthermore, a temperature of 1200°C is reached in the thickest points of the profile. The temperature changes can be interpreted as local variations in viscosity based on Eq. 4, which was defined previously. Figure 5c shows viscosity values in kg m$^{-1}$ s$^{-1}$. The viscosity values are defined in different regions by Eq. 4 and represented on $S_4$ transverse plane. As shown in the figure, viscosity values close to the solidification imposed by the model ($\sim 1 \times 10^{14}$ kg m$^{-1}$ s$^{-1}$) are reached at the extremes of the ribbon with thicknesses approximately corresponding to 19.5 $\mu$m. However, in the region where the thicknesses exceed the average, the viscosity still does not reach critical values for solidification. Thus, the metal mass ejected in the CBMS process can still flow. The temperature of the lower zone of contact with the wheel is lower compared to the rest of the profile (see Fig. 5b). In the central zone, a difference in viscosity of approximately 1000 kg m$^{-1}$ s$^{-1}$ (see
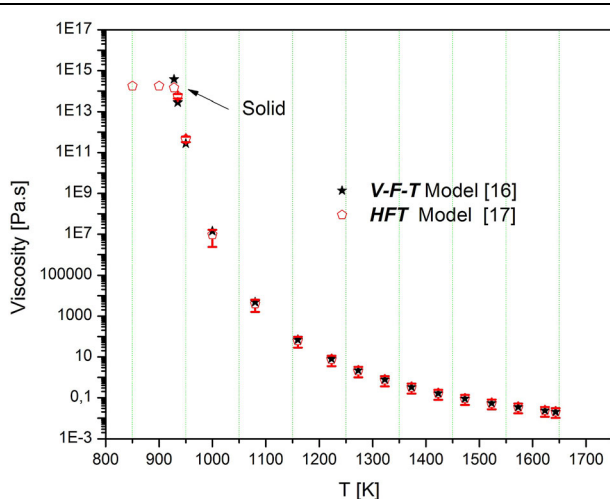


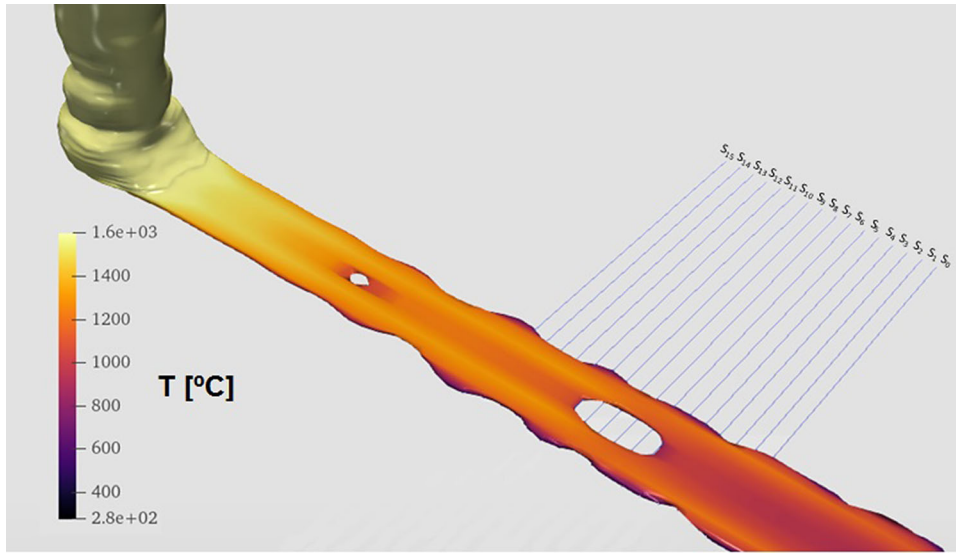Fig. 2. Thicknesses obtained with the HTE model and different reported experimental values.

Fig. 3. Simulation in OPENFOAM® of a CBMS process turbulent zone during shaping of a $Fe_{78}Si_9B_{13}$ (at.%) ribbon ejected with a gap of 2 mm over a rotating copper wheel. Sectioning planes $S_i$ with $i$ = 0–15 considered within the main study zone.
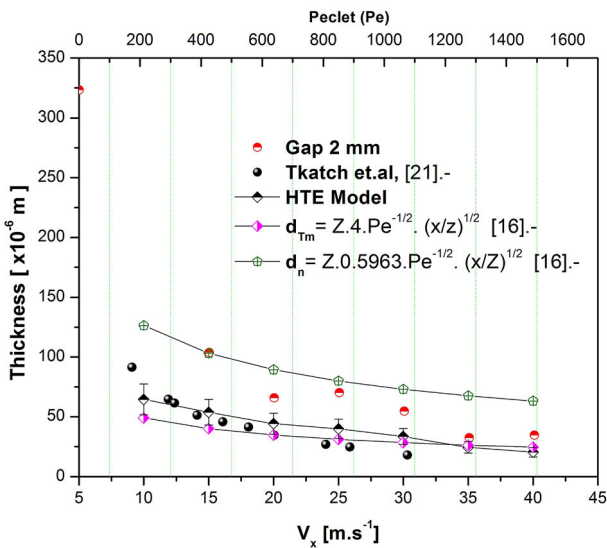


Fig. 4.. Viscosity temperature-dependent graph comparative values proposed by VFT and HTE models.

Fig. 5c) leads to more fluid layers of metal for consolidation in the upper part. The fluid zone exhibits vortices with speeds in the range of 6–7 times that of the expulsion speed of the alloy in the nozzle.[14] This results in a central region with a thickness lower than the average thickness, as shown in Fig. 5a. The fluidity of the central mass leads to a trapped bubble with an approximate diameter of $1.7 \times 10^{-4}$ m (see Fig. 1) in the region that deforms because of vorticities and surface tension ($\sigma$) effects at high temperatures (approximately 1300°C). This causes a depression h (approximately $-1.14 \times 10^{-5}$ m) with a contact angle of 90.27° in the upper part of the profile. This is shown in the cross section analyzed later (see Fig. 6). A thin section with a width in the order of the previous bubble ($\sim 1.5 \times 10^{-4}$ m) and thickness of approximately 8 $\mu$m (see Fig. 6a) is increasingly more viscous from the bottom, and temperatures correspond to 900–1000°C. The thin section collapses because of the action of the vorticities described in the regions close to the critical length and inertia resulting from the melt after ejection onto the rotating wheel. The solidification during the collapse of the thin section determines the growth of the crack in an irregular manner. The solidification begins in its lower plane, which is more viscous than its upper part (see details in Fig. 6c). Conversely, the fluidity of the melt on the sides (left and right) can still be observed in areas with viscosities below approximately 100 kg $m^{-1}$ $s^{-1}$. Subsequently, the joint action of the material that flows down the sides of the crack and that in the central and extreme regions of the ribbon begins to solidify, thereby causing the crack to display a width of $3.1 \times 10^{-4}$ m in the cross section (see Fig. 7a). The value is very close to that observed experimentally, approximately $2.5 \times 10^{-4}$ m (see Fig. 1). As shown in Fig. 7c, in this region, a difference in viscosity (approximately 1000 kg $m^{-1}$ $s^{-1}$) continued to exist in areas denoted with arrows. The region is not solidified given the absence of a reduced thickness (approximately 27 $\mu$m) compared to profile extremities (approximately 13 $\mu$m) and because local temperatures are close to 1100°C (see Fig. 7b).

The action of the inertial force on the sides of the crack (where more mass is concentrated because of increases in thickness and temperature) changes the Reynolds number (Re) values of the fluid areas to those that denote turbulent flow (Re $\sim$ 3519). This in turn leads to advancement of the molten material to the adjacent sections.
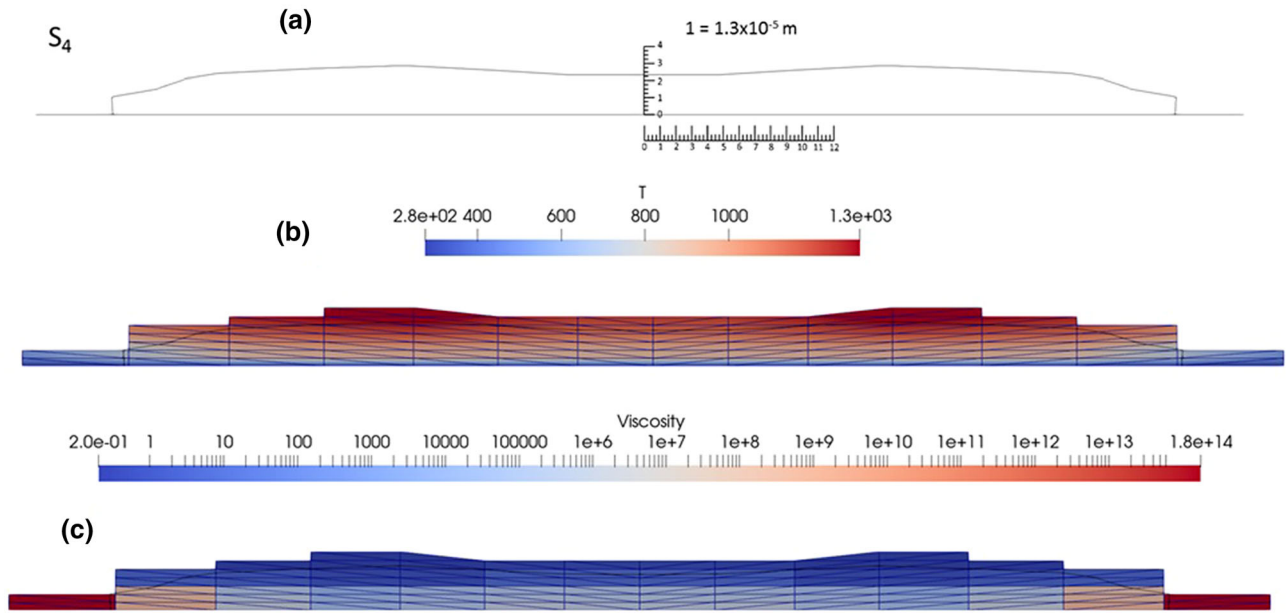
Fig. 5. Sectioning plane $S_4$ with: (a) thicknesses obtained in the profile (scale: $1 = 1.3 \times 10^{-5}$ m), (b) temperatures obtained in the profile (scale in °C), and (c) dynamic viscosities obtained in the profile with solidification at extremes (scale in Pa s).
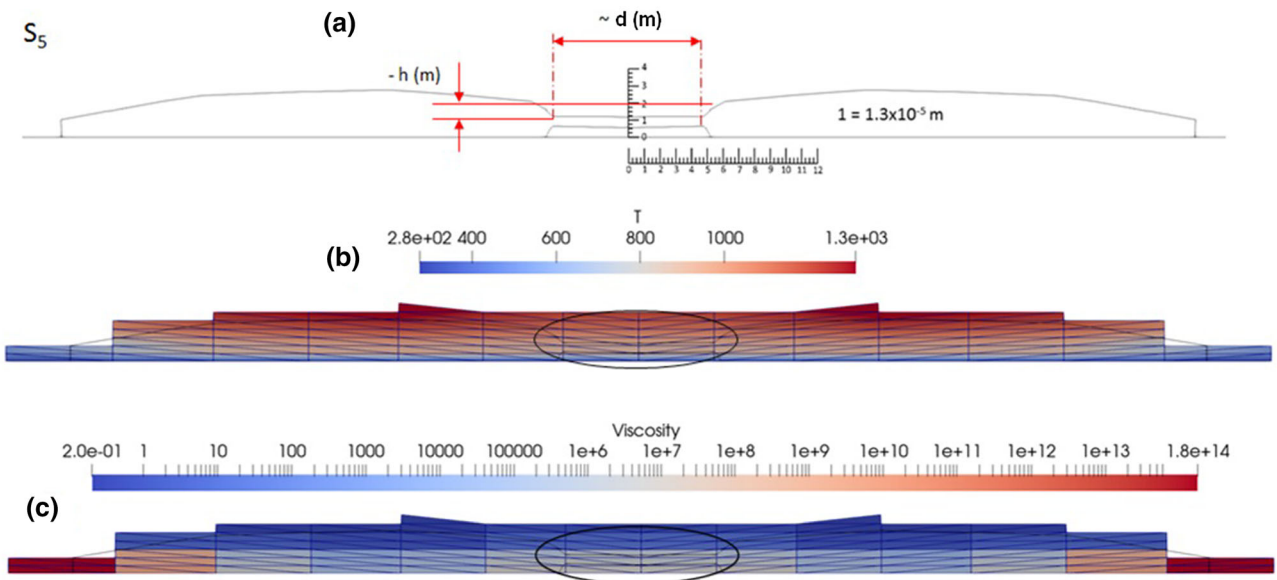


Fig. 6. Sectioning plane $S_5$ with: (a) thicknesses obtained in the profile with details of depression ($-h$) and width (L) of thinning (scale: $1 = 1.3 \times 10^{-5}$ m). (b) Temperatures obtained in the profile with details of thinning (scale in °C). (c) Dynamic viscosities obtained in profile with details of thinning and solidification at the ends (scale in Pa s).

Hence, the material flows towards section $S_{11}$ where the entire ribbon layer is formed given the contribution from the upper layers of molten metal with viscosities corresponding to approximately $2 \times 10^{-1}$ kg m$^{-1}$ s$^{-1}$. This defines a homogeneous film profile with an average thickness of 27.5 $\mu$m (see Fig. 8) when the bubble collapses. Additionally, the solidification profile around the area of the crack continues to consolidate from the center and extremes of the ribbon. There the thicknesses are

less than the obtained average values. It is observed that in the central zone already solidified lower planes coexist with a viscosity of $1.5 \times 10^{14}$ kg m$^{-1}$ s$^{-1}$ and upper planes with a viscosity of 10 kg m$^{-1}$ s$^{-1}$.

Hence, in the profile, the upper ribbon planes continue to be fluid. This is because the temperatures are high (approximately 1200°C) given the proximity to the crucible (or molten pool), as shown in Fig. 3.
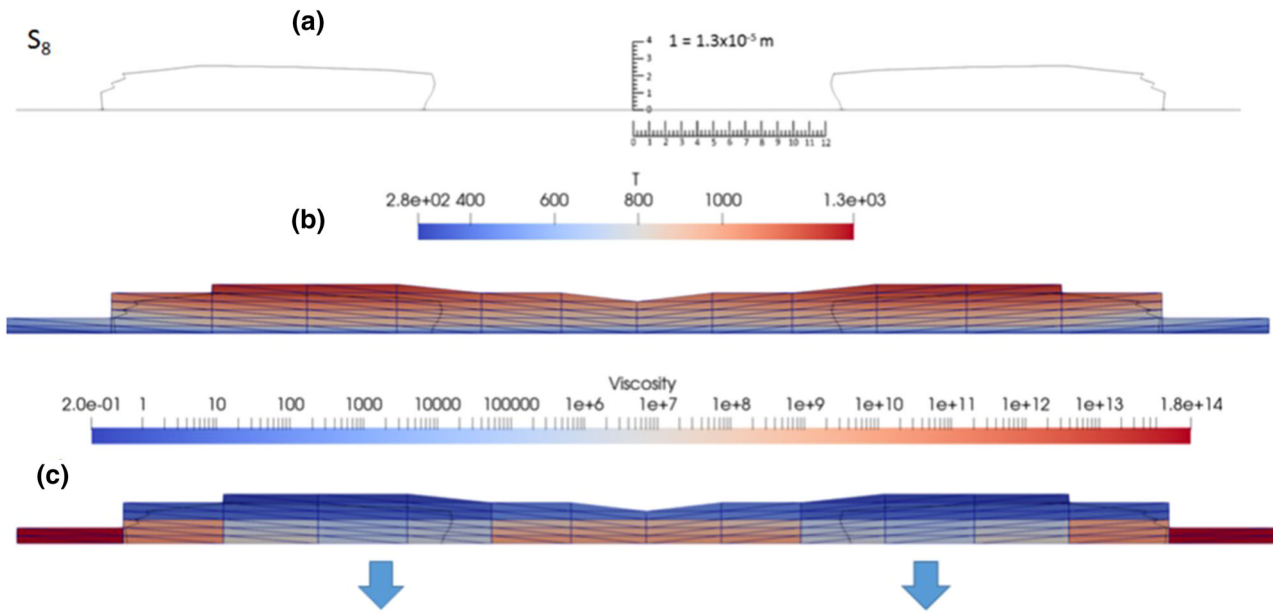
Fig. 7. Sectioning plane $S_8$ with: (a) thicknesses obtained in the profile with central cracking (scale: $1 = 1.3 \times 10^{-5}$ m); (b) temperatures obtained in the profile (scale in °C); (c) dynamic viscosities obtained in the profile with details of fluidity regions (arrows) in areas not yet solidified and with solidified extremes (scale in Pa s).
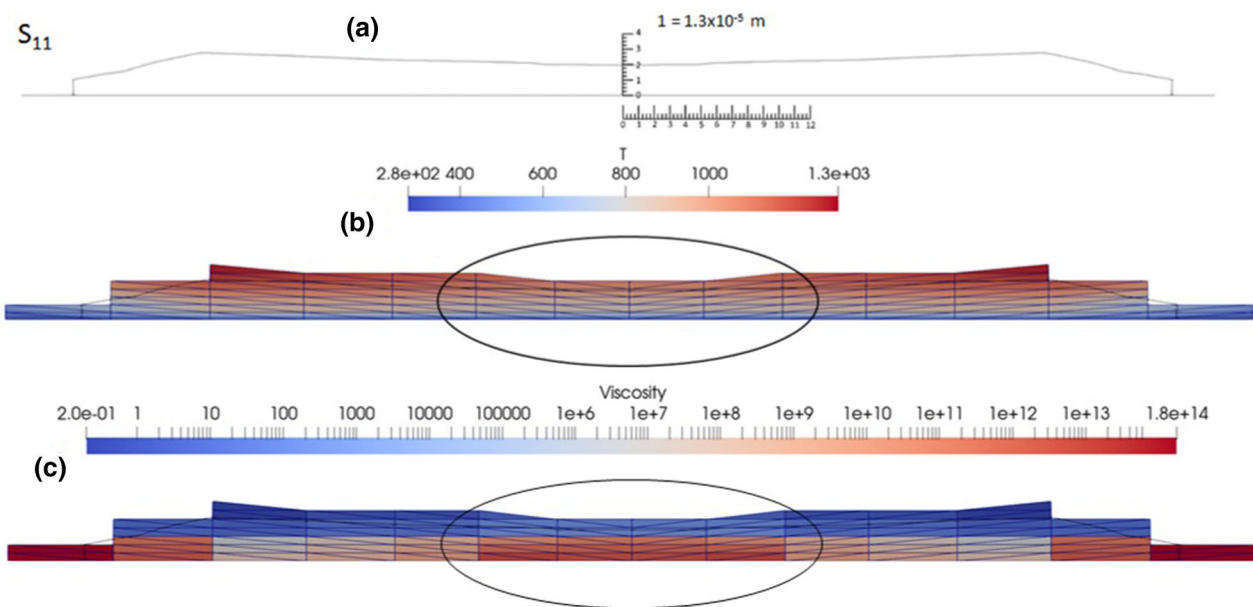


Fig. 8. Sectioning plane $S_{11}$ with: (a) thicknesses obtained in the profile (scale: $1 = 1.3 \times 10^{-5}$ m), (b) temperatures obtained in the profile with details in the central area (scale in °C), and (c) dynamic viscosities obtained in the profile with details in the central solidified zone and extremes (scale in Pa s).

## Specific Discussion

In "Experimental" section, a bubble with an approximate diameter of $1.5 \times 10^{-4}$ m, which is trapped in the solidification ribbon profile, is reported. This suggests that it can be deformed because of vorticities in the surrounding atmosphere and surface tension effects. Both effects can generate a crack that evolves according to the complex solidification mechanism described in

"General Discussion" section. This is conformed because $Bi_{s/l} > 1$ and $Bi_A > 7.5 \times 10^{-4}$ in relation to the speeds $V_x$ of our process, and thus the ribbon cooling is affected by vorticities observed in the regions.[14,24] Additionally, in the same range of rotation of the copper wheel that is examined in this work, other studies observed an increase in the formation of surface bubbles associated with the trapping of gas at the liquid-wheel interface.[13,25]

The conditions are highly probable in our process, and they are observed when possible dimensions of r (m) bubbles are calculated, which can be trapped in this condition as follows.

For $\Delta P$ = 70,000 N m$^{-2}$ and $\sigma$ = 1.2 N m$^{-1}$[17] in Eq. 5:

$$\Delta P = \frac{4.\sigma}{r}. \tag{5}$$

In the CBMS process, diameters (2.r) can be obtained, and in this case the diameter corresponds to $1.37 \times 10^{-4}$ m. A comparable magnitude is observed in Fig. 1. The magnitude can be deformed by the action of a complex balance among vorticity, surface tension, and viscous and inertial forces. These actions begin to manifest themselves in the thinning described during solidification (see Fig. 6). The solidification determines growth of irregularly shaped cracks. Viscous forces and surface tension in regions at different temperatures, as listed in Table I, can be used to determine the value of the corresponding dimensionless number that links them as follows:

$$Ca = \frac{\mu.v}{\sigma} \tag{6}$$

where $\mu$ = dynamic viscosity (Pa s), v = Velocity (m s$^{-1}$), $\sigma$ = Surface tension (N m$^{-1}$).

As shown in Table I, at approximately 1300°C, the effects of the viscous forces are no longer significant, and the effects of surface tension are evident only at 50°C above the aforementioned value. Hence, the following expression is obtained.

$$Ca = \text{viscous forces/surface tension forces} \tag{7}$$

Then, the role of the inertial forces at the sides of the crack determines the fluid column advancement between two regions: the extremes of the ribbon profile (that are solidifying) and thinning or collapsing film inside the crack, which forms because of the action of the same forces. The role is demonstrated by examining the dimensionless Weber number (We), which arises from the following expression:

**Table I. Table of dynamic viscosity values and dimensionless numbers Ca**

| T (°C) | μ (Pa s) * | Ca ** |
| --- | --- | --- |
| 950 | 7.4631 | 248.773 |
| 1000 | 2.0918 | 69.726 |
| 1200 | 0.0892 | 2.973 |
| 1300 | 0.0343 | 1.143 |
| 1350 | 0.0233 | 0.776 |

*Dynamic viscosity obtained with HTE model.[15] **Dimensionless number Ca = f (T).

$$Ca = \frac{We}{Re} \tag{8}$$

which corresponds to

$$We = \text{inertial forces/surface tension forces.} \tag{9}$$

Subsequently, we obtain a We of approximately 2700 if the Re number in the same region is known. This indicates the dominance of the inertial forces over surface tension in these areas. Therefore, we can also infer that these forces cause the thin fluid layer to disintegrate in the thinning case (Fig. 6a). The cracking gap is registered in the center cross-section $S_8$ (see Fig. 7a) after the bubble collapses.

## CONCLUSION

In this study, we used a VOF model implemented in OPENFOAM$^{®}$ for two non-isothermal, immiscible, and compressible fluids using compressibleInterFoam to solve a mathematical model with a hyperbolic tangent-type viscosity function (HTE model), which was previously assigned to the solver to recreate the required turbulence condition to explain the bubble formation in the CBMS process of $Fe_{78}Si_9B_{13}$ (at.%). Specifically, the ribbon was ejected with a 2-mm gap over the rotating copper wheel. The dimensionality of the modeled crack (in the range of $1.24 \times 10^{-4}$–$3.1 \times 10^{-4}$ m) was verified by comparing it with a real cracking obtained in an experimental laboratory process (in the range of $1.7 \times 10^{-4}$–$2.5 \times 10^{-4}$ m). The results also indicated that the effects of viscous forces were significant at 1200°C. At this temperature, the surface tension is almost tripled, temperatures exceed 1300°C, and the effects of both forces tend to balance out. Above this temperature, the surface tension prevails over the viscous stresses. The fine balance of forces in the range of 1000–1350°C (together with the vorticity in the liquid-solid contact zone) resulted in the formation of a narrow section, which led to cracking from a trapped bubble in the FeSiB ribbon (see Figs. 7 and 8). Subsequently, the bubble collapsed because of the inertial force (We $\sim$ 2700). The transverse profile solidification, at cooling rates described in the laboratory tests in the study ($\sim 9.3 \times 106$ K s$^{-1}$), and trapped gas pockets, which affected profile roughness, were consistent with those obtained in other studies.[13,16,18,20] This effect reinforced the hypothesis of the molten material pool formation proposed in the present study.

## CONFLICT OF INTEREST

The authors declare that they have no conflict of interest.

## REFERENCES

1. M. Carlen, D. Xu, J. Clausen, T. Nunn, V.R. Ramanan, and D.M. Getson, *IEEE Pes T&D*. https://doi.org/10.1109/TDC.2010.5484301 (2010).
2. Mariusz Najgebauer, Krzysztof Chwastek, Jan Szczygłowski, PRZEGLĄD ELEKTROTECHNICZNY, R. 87 NR 2/2011, ISSN 0033-2097.
3. R. Hasegawa, and D. Azuma, *J. Magn. Magn. Mater.* 320(20), 2451 (2008).
4. D. Azuma, N. Ito, and M. Ohta, *J. Magn. Magn. Mater.* 501, 166373 (2020).
5. G.-X. Wang, and E.F. Matthys, *Modelling Simul. Mater. Sci. Eng.* 10, 35 (2001).
6. P.H. Steen, and C. Karcher, *Annu. Rev. Fluid Mech.* 29, 1. (1997).
7. K. Suzuki, A. Makino, A. Inoue, and T. Masumoto, *J. Applied Physics.* 70, 6232 (1991).
8. D. Muraca, J. Silveyra, M. Pagnola, and V. Cremaschi, *J. Magn. Magn. Mater.* 321(21), 3640 (2009).
9. Y. Nomura, J. Uzuhashi, T. Tomita, T. Takahashi, H. Kuwata, T. Abe, T. Ohkubo, and K. Hono, *J. Alloys Comput.* 859, 157832 (2021).
10. M. Pagnola, S. Preckel, H. Alvarez Barrios, Development of Numeric Simulation Model for Production Control a Melt Spinning Process of Amorphous Ribbon Used in Transformer Cores. Paper presented at the 2nd International Conference on Materials, Mechatronics and Automation, Hanbat National University, Korea, 22–24 November 2012.
11. M.R. Pagnola, M. Malmoria, M. Barone, and H. Sirkin, *MMMS* 10(4), 511 (2014).
12. A.G. Marrugo, M. Barone, J. Useche, M. Pagnola, OSA. The Optical Society, Paper LTh2C.5. (2016).
13. R.E. Napolitano, and H. Meco, *Metal. Mater Trans A* 35, 1539 (2004).
14. M. Pagnola, M. Malmoria, and M. Barone, *ATE* 103(1), 807 (2016).
15. M. Barone, F. Barceló, J. Useche, A. Larreteguy, and M. Pagnola, *UIS* 17(1), 185 (2017).
16. C. Wang, *Numerical Modeling of Free Surface and Rapid Solidification for Simulation and Analysis of Melt Spinning* (Iowa State University-Ames, Iowa, 2010), pp 1–138.
17. M. Barone, F. Barceló, M. Pagnola, A. Larreteguy, A. Marrugo, and J. Useche, *Int. J Therm. Sci.* 150, 106221 (2020).
18. J. Carpenter, and P. Steen, *Int. J. Heat Mass Transf.* 40(9), 1993 (1997).
19. M. Pagnola, M. Barone, M. Malmoria, and H. Sirkin, *MMMS* 11(1), 23 (2015).
20. G. Wang, and E. Matthys, *Model. Simul. Mater. Sci. Eng.* 10(1), 35 (2002).
21. V.I. Tkatch, A.I. Limanovskii, S.N. Denisenko, and S.G. Rassolov, *Mater. Sci. Eng. A* 323(1–2), 91 (2002).
22. G. Pozo Lopez, L.M. Fabietti, A.M. Condo, and S.E. Urreta, *JMMM* 322(20), 3088 (2010).
23. Y. Takata, H. Shirakawa, H. Sasaki, T. Kuroki, and T. Ito, *Scripta Technica Heat Trans Asian Res.* 28(1), 34 (1999).
24. M. Bussman, J. Mostaghimi, D.W. Kirk, and J.W. Graydon, *Int. J. Heat Mass Transf.* 45(19), 3997 (2002).
25. R. Dhadwal, *Appl. Math. Model.* 35(6), 2959 (2011).